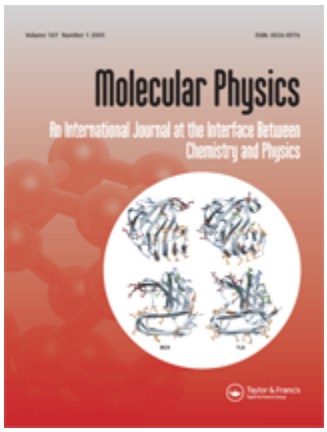

Fourier transform spectroscopy of HD in the Extreme Ultraviolet at $\lambda= 87-112$ nm

Journal:	*Molecular Physics*
Manuscript ID:	TMPH-2009-0355.R1
Manuscript Type:	Special Issue Paper -HRMS Stabia 09/ High Resolution Molecular Spectroscopy
Date Submitted by the Author:	15-Jan-2010
Complete List of Authors:	Ivanov, Toncho; Laser Centre Vrije Universiteit Amsterdam, Atomic and molecular Physics Dickenson, Gareth; Laser Centre Vrije Universiteit Amsterdam, Atomic and molecular Physics ROUDJANE, Mourad; Observatoire de Paris-Meudon, LERMA de Oliveira, Nelson; Synchrotron Soleil, DESIRS Joyeux, Denis; CNRS, Laboratoire Charles Fabry de l'Institut d'Optique Nahon, Laurent; Synchrotron Soleil, DESIRS Tchang-Brillet, Wan-Ü; Observatoire de Paris-Meudon, LERMA Ubachs, Wim; Laser Centre Vrije Universiteit Amsterdam, Atomic and molecular Physics
Keywords:	fourier-transform spectroscopy, HD, fundamental constants, High precision spectroscopy, hydrogen deuteride
Note: The following files were submitted by the author for peer review, but cannot be converted	

HD-synchrotron.tex
HD-synchrotron.bbl

Molecular Physics
Vol. 00, No. 00, Month 200x, 1–17

RESEARCH ARTICLE

Fourier-Transform spectroscopy of HD in the Vacuum Ultraviolet at $\lambda = 87 - 112$ nm

T.I. Ivanov[a], G.D. Dickenson[a], M. Roudjane[b†], N. de Oliveira[b], D. Joyeux[bc], L. Nahon[b], W.-Ü L. Tchang-Brillet[de], W. Ubachs[a*]

[a]Laser Centre, Vrije Universiteit, De Boelelaan 1081, 1081 HV Amsterdam, The Netherlands
[b]Synchrotron Soleil, Orme des Merisiers, St Aubin BP 48, 91192 GIF sur Yvette cedex, France
[c]Laboratoire Charles Fabry de l'Institut d'Optique, CNRS, Univ Paris-Sud Campus Polytechnique, RD128, 91127, Palaiseau cedex, France
[d]Laboratoire d'Étude du Rayonnement et de la Matière en Astrophysique, UMR 8112 du CNRS, Observatoire de Paris-Meudon, 5 place Jules Janssen, 92195 Meudon cedex, France
[e]Université Pierre et Marie Curie-Paris 6

(*January 15, 2010*)

Absorption spectroscopy in the vacuum ultraviolet (VUV) domain was performed on the hydrogen-deuteride molecule with a novel Fourier-Transform spectrometer based upon wave-front division interferometry. This unique instrument, which is a permanent endstation of the undulator-based beamline DESIRS on the synchrotron SOLEIL facility, opens the way to Fourier-Transform spectroscopy in the VUV range. The HD spectral lines in the Lyman and Werner bands were recorded in the 87-112 nm range from a quasi-static gas sample in a windowless configuration and with a Doppler-limited resolution. Line positions of some 268 transitions in the $B^1\Sigma_u^+$ $(v' = 0-30) \leftarrow X^1\Sigma_g^+$ $(v'' = 0)$ Lyman bands and 141 transitions in the $C^1\Pi_u(v' = 0-10) \leftarrow X^1\Sigma_g^+(v'' = 0)$ Werner bands were deduced with uncertainties of 0.04 cm$^{-1}(1\sigma)$ which correspond to $\Delta\lambda/\lambda \sim 4 \times 10^{-7}$. This extensive laboratory database is of relevance for comparison with astronomical observations of H_2 and HD spectra from highly redshifted objects, with the goal of extracting a possible variation of the proton-to-electron mass ratio ($\mu = m_p/m_e$) on a cosmological time scale. For this reason also calculations of the so-called sensitivity coefficients K_i were performed in order to allow for deducing constraints on $\Delta\mu/\mu$. The K_i coefficients, associated with the line shift that each spectral line undergoes as a result of a varying value for μ, were derived from calculations as a function of μ solving the Schrödinger equation using *ab initio* potentials.

1. Introduction

The $B^1\Sigma_u^+$ - $X^1\Sigma_g^+$ Lyman bands and the $C^1\Pi_u$ - $X^1\Sigma_g^+$ Werner bands are the strongest electronic absorption systems in the hydrogen molecule. The electronic transition relates to the $1s - 2p$ transition in the hydrogen atom, also known as the Lyman-α line. In the molecular case the $2p$-orbital is either aligned along the molecular axis, the $2p\sigma_u$-orbital giving rise to the $B^1\Sigma_u^+$ state, or perpendicular to the molecular axis, the $2p\pi_u$ orbital, giving rise to the doubly degenerate $C^1\Pi_u$ state; the latter degeneracy is lifted by non-Born-Oppenheimer effects (Λ-doubling)

†present adress : Department of Chemistry, 009 Chemistry-Physics Building, University of Kentucky, 505 Rose Street, Lexington, KY 40506-0055, USA
*Corresponding author. Email: wimu@few.vu.nl

ISSN: 0026-8976 print/ISSN 1362-3028 online

DOI: 10.1080/002689700xxxxxxxxxxx
http://www.informaworld.com

giving rise to non-degenerate $C^1\Pi_u^+$ and $C^1\Pi_u^-$ states. Band structure is imposed due to the rotational and vibrational substructure of the excited states, while in most absorption studies only a few rotational states are populated in the lowest $X^1\Sigma_g^+$ ($v = 0$) rovibronic ground state. The absorption spectrum of the Lyman and Werner bands in the hydrogen molecule are blue-shifted from the atomic Lyman-α transition at $\lambda = 121$ nm. This is understood from the fact that the binding energies in the $B^1\Sigma_u^+$ and $C^1\Pi_u$ states are less than in the $X^1\Sigma_g^+$ ground electronic state. Hence the molecular absorption spectrum falls in the VUV-domain starting at $\lambda = 112$ nm and progressing towards shorter wavelengths.

Because hydrogen is the most abundant molecular species in the universe, the strong Lyman and Werner band systems are ubiquitiously observed in outer space. Nevertheless it took until 1970 for the first observation of molecular hydrogen in space was reported by Carruthers [1] using a rocket borne spectrometer observing from high altitudes, therewith evading atmospheric absorption of the vacuum ultraviolet radiation. Soon thereafter molecular hydrogen was also observed in the line of sight of highly redshifted quasars [2, 3]. More recently in addition to the main H_2 isotopomer also the hydrogen deuteride molecule has been detected in quasars [4–6]. A special feature of the HD isotopomer is the phenomenon of breaking of the inversion symmetry, or the mixing between states of *gerade* and *ungerade* symmetry [7]. One effect of this phenomenon is the interaction between $B^1\Sigma_u^+$ and $C^1\Pi_u$ states with $EF^1\Sigma_g^+$ states, lending intensity for absorption in the $EF - X$ system in HD.

A seminal study on the absorption and emission spectra of the Lyman and Werner systems in HD has been performed by Dabrowski and Herzberg using a classical grating spectrograph [8]. The resolution obtained in this Doppler-limited study was 1.0 cm^{-1}, while the accuracy of the line positions was several 0.1 cm^{-1}. Some twenty years later the spectroscopy of some of the Lyman and Werner bands was reinvestigated using a tunable laser system in the vacuum ultraviolet and excitation in a molecular beam [9], thus lowering the resolution to 0.25 cm^{-1} and the absolute accuracy to below 0.1 cm^{-1}. Recently the spectra in the range $\lambda = 100 - 112$ nm were re-investigated with the use of an improved VUV-laser system, yielding spectral linewidths of 0.02 cm^{-1} and absolute accuracies of 0.005 cm^{-1} [10]. Previously the $B - X(v', 0)$ Lyman bands had been investigated for $v' = 0 - 2$ [11] and for $v' = 15$ [12] at this high accuracy. The region near the ionization threshold in HD had been investigated at high resolution employing a narrowband VUV laser[13].

Motivated by the need for accurate wavelength positions and in order to extract tight constraints on the variation of the proton-to-electron mass ratio from quasar absorption data [14–16], now that also spectral lines of HD have been observed and may be included in the analysis [4–6], we set out to reinvestigate the VUV absorption spectrum of HD. The broadly covering investigation of Dabrowski and Herzberg [8] does not have sufficient accuracy, *i.e.* is less accurate than the high redshift lines obtained from astronomical observation. At the same time the laser investigations [9–12] lack the broad coverage and still some gaps exist in the knowledge of the laboratory data of HD.

The availability of the novel Fourier-Transform spectrometer in the vacuum ultraviolet range allowed us to remeasure in HD the Lyman absorption bands up to $v' = 30$ and the Werner bands up to $v' = 10$. Wavelength positions of over 400 lines in the HD absorption spectrum were determined with an uncertainty of 0.04 cm^{-1}, or $\Delta\lambda/\lambda = 4 \times 10^{-7}$. The internal calibration of the FT instrument was improved during the course of the investigation through the use of the previously laser-calibrated lines of HD(at the 5×10^{-8} level) in the ranges where they are available. As such the present investigation is also a test of the accuracy and the

capabilities of the unique FT-instrument in the VUV-domain.

Methods to determine constraints on a variation of the proton-to-electron mass ratio from spectral lines in molecules require three ingredients. Besides the spectral line positions observed at high redshift, and an accurate laboratory data set of wavelengths, also knowledge is required on the value of the sensitivity coefficients that determine how far lines will shift as a result of a change in mass ratio. For the case of H_2 such sensitivity coefficients were calculated by semi-empirical methods [15, 17], and alternatively by *ab initio* calculations [18]. In a previous study on the laser calibration of part of the HD spectrum calculations of some sensitivity coefficients were reported [10]. In the present paper such calculations are further detailed and extended to the broad coverage of the spectrum.

2. Experimental setup

Absorption spectra of the hydrogen deuteride molecule HD have been recorded in the $\lambda = 87 - 112$ nm range using a Fourier-Transform (FT) spectrometer, which is installed as a permanent endstation on the VUV undulator-based DESIRS beamline on the French synchrotron facility SOLEIL [19]. The FT-instrument is the first of its kind to achieve high resolution transmission spectra in this short-wavelength windowless regime. Previously, with the aid of optical beam-splitters to perform amplitude-division interferometry for dividing paths in the Michelson configuration, a Fourier-Transform spectrometer had been operated at wavelengths as short as λ=140 nm [20]. With the here described unique instrument the advantageous properties of FT-spectroscopy, the capability to reach high spectral resolving power $\lambda/\Delta\lambda$ as well as the multiplex capability, are extended to wavelengths beyond the MgF_2 cutoff. This can be accomplished by replacing the amplitude-division concept by a wavefront-division method in obtaining interferograms. The present recordings of high resolution spectra of HD serve also as a demonstration of the obtainable accuracies on wavelengths positions of spectral lines with the novel instrument, owing to the availability of a multitude of accurately calibrated lines from laser experiments.

The FT-spectrometer can achieve an ultimate theoretical resolving power of around 1 million over the entire VUV spectral range covered by the instrument (40-180 nm), which is between 5 and 10 times better than the capabilities of state of the art VUV grating-based spectrometers. A first version of the VUV FTS, operating in the mid-UV range, has been described in detail [21]. Although the underlying physical principles are similar, the DESIRS instrument has been improved and can now be operated in the 40-180 nm range (6-30 eV). Here we give a brief description on the main features of operation of the instrument, relevant to the current study, while a more complete report is in preparation [22].

The interferometer is based upon a modified design of the traditional Fresnel bimirror interferometer. Two roof reflectors, separated by a 100 μm gap and having an angle of 0.35 mrad between each other are illuminated in the vicinity of the gap by the coherent synchrotron radiation beam encoded with information on the HD absorption features. The reflected beams from both reflectors then overlap and interfere at the plane of the detector located at a distance of 1.3 m. The inteferometric signal is recorded continuously at equal path difference intervals by translating one of the reflectors. The source spectral distribution is then recovered by performing a Fourier transformation onto the recorded interferogram. Working in the VUV range requires special care, since optical and mechanical tolerances are directly related to the operation wavelength. Therefore the motion of the reflector is controlled by a sophisticated system which has been especially developed for the

VUV FTS. Briefly, it consists of a highly sensitive multireflection deflectometer and a multipass Michelson interferometer, both employed to ensure that the required precision is achieved.

As it is important for the recalibration and the error estimation procedures, the multireflection Michelson interferometer is briefly described hereafter (a more detailed description can be found elsewhere [19, 23]). The still reflector has its back side fixed to a stable solid optical block while the back surface of the moving reflector creates a small angle with respect to the surface of the optical block, thus creating a small angle air wedge (fig. 1). When inserting a He-Ne laser beam probe in this wedge with an appropriate entrance angle, the laser beam can be exactly retro-reflected and overlapping the entrance path (after p reflections between the two planes of the wedge as shown in the inset of Fig. 1). This multireflection set-up is the moving arm of a traditional Michelson interferometer used here as a control system. The sinusoidal interferometric signal period given by the interferometer is then directly related to the p parameter. Owing to the multireflection amplification, the period of the signal is roughly inversely proportional to the number of reflections p, namely, period $\approx \lambda_{laser}/2p$ (note that this is the period in terms of the displacement of the moving reflector). The VUV interferometric signal is then triggered at regular path difference steps following a sampling comb generated from the HeNe interferometric signal (twice per signal period). The p parameter can be set in-situ in the 7 to 16 range. This allows to adapt the sampling interval of the interferogram as a function of the smallest wavelength in the spectrum in order to have at least two points per fringe (Nyquist condition). This is a powerful way to keep the relative spectral resolution close to the maximum value, determined by the number of recorded samples, over a large spectral range.

Ideally, the geometry of the control system is perfectly known, and therewith the value of the sampling interval for a given p as well. Hence, the spectral scale is also perfectly determined for each value of p. In practice, some geometrical parameters are not well known, and are difficult to measure. The consequence is that the spectral calibration deviates from the ideal values, the deviation being p-dependent and in the order of a few 10^{-7}. Most of the measurements in the present study were done at $p = 8$ and a minor part at $p = 7$.

OPHELIE2, the undulator feeding the DESIRS beamline provides a VUV pseudo-white radiation with a broadband Gaussian-like spectrum with a $\delta E/E$ relative spectral bandwidth of 7%. The position of the spectral window can be

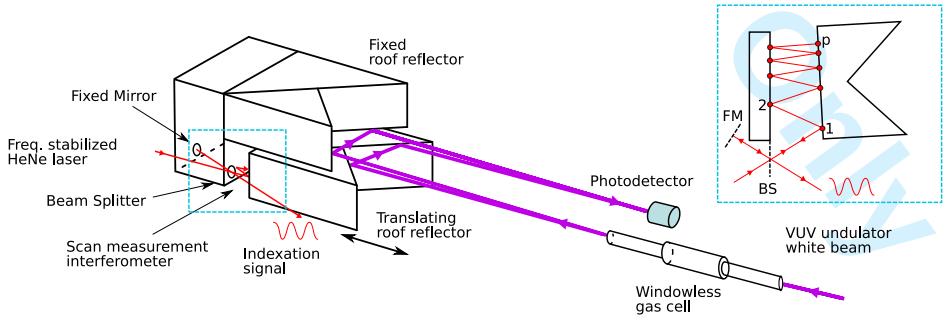

Figure 1. Experimental layout of the VUV FT spectrometer setup. The VUV wavefront division interferometer is facing the VUV synchrotron beam. The two roof-shape reflectors are slightly tilted in order to make the two reflected beams overlap and interfere on a photodiode. A part of the scanning measurement setup is shown on the back side. The incident frequency-stabilized HeNe laser beam is splitted by a beam splitter (BS), the reference beam is reflected at normal incidence by a plane fixed mirror (FM), the transmitted beam is reflected p times between the back of the moving VUV reflector and a plane mirror part of the reference optical block that includes the fixed VUV reflector. All the fixed optical elements are part of the same optical block in order to minimize possible differential errors. The multireflection setup ensures the required high sensitivity for the movement indexation.

easily tuned over the whole VUV range, by tuning the magnetic field of the undulator, operated in the linear vertical polarization mode [24]. Only the fundamental radiation of the undulator is used. The higher harmonics are being cut-off by a free flow gas filter acting as a low-energy pass filter [25]. The undulator white beam is only reflected by three mirrors at a 20 deg grazing incidence angle before entering the FTS, ensuring a high spectral brightness. This is the relevant photometric parameter for wavefront-division interferometry as this technique requires a high density spatially coherent photon flux. The broad bandwidth synchrotron beam is then sent towards a differentially-pumped multipurpose gas sample chamber, containing the sample. The measured HD gas is introduced into a free flow windowless T-shaped gas cell, which consists of a cylindrical steel tube 100 mm long and 30 mm inside diameter. This configuration leads to an inhomogeneous density distribution along the direction of the synchrotron radiation beam. By regulating the pressure at the gas cell input an integrated column density up to a few times 10^{18} particles per cm^2 can be achieved. Beyond the interaction with the gas the synchrotron light is used as an input source for the FTS.

Interferograms are recorded "on the fly", *i.e.* sampling is performed during the continuous translation of the moving arm of the interferometer yielding a typical scan time of 3 minutes, during which 512 Ksamples are aquired. Each final spectrum at a certain column density represents a summation over 100 individual spectra. The total time to acquire such spectrum spanning over 5000 cm^{-1} is approximately two hours. Fig. 2 shows an example of such averaged spectrum.

All measurements were done at room temperature, where the Doppler width for HD is $0.7 - 0.8$ cm^{-1}. Therefore the ultimate instrumental resolution is not needed. Instead, it was optimised to gather a sufficient amount of points per spectral line and keep the collection time for an interferogram as low as possible so it can be used for improving the signal to noise ratio (S/N is proportional to the square root of the number of averaging individual spectra). For the present study an optimized measurement time/resolution conditions with an acceptable S/N ratio were achieved by setting the instrumental line width between 0.3 and 0.4 cm^{-1} corresponding to a resolving power of about 350000.

It is worth mentioning that the capabilities of the FTS were not fully exploited due to a relatively poor signal-to-noise ratio in some of the spectral regions covered by the instrument. FTS is a photon noise-limited technique and the S/N ratio obtained is proportional to the square root of the photon flux. The latter was sub-optimal due to slight misalignment and especially due to small amounts of carbon contamination on some of the FTS and beamline optics giving rise to absorption in the spectral region of interest.

3. Experimental results and discussion

Some 400 absorption lines of the Lyman and Werner bands of HD have been measured with absolute accuracies of 0.04 cm^{-1} (*i.e.* 4×10^{-7} relative accuracies). The transition frequencies are presented in Table 1 for the Lyman bands and Table 2 for Werner bands, respectively. Some of the line positions have previously been calibrated at better accuracies - 5×10^{-8} [10–12], while Hinnen *et al.* [9] performed a lower resolution laser based study with a claimed accuracy of 3.5×10^{-7}. For the remainder the best results known are those from Dabrowski and Herzberg [8] with accuracies of few $\times 10^{-6}$. The present results therefore yield an order of magnitude improvement in accuracy for the majority of the lines.

The spectral range 90000-115000 cm^{-1} was divided into five different measurements regions, each covering around 5000 cm^{-1}. In order to have sufficiently strong

but saturated absorption features for each transition with rotational number up to $J = 5$, scans at several column densities for each spectral region are necessary. We have performed measurements at four different column densities for each spectral window, taking into account that the bands tend to become stronger towards shorter wavelength.

A Fourier-Transform spectrum is characterised by a constant noise level determined ideally by the photon flux reaching the detector and the number of averaged individual spectra. Each spectral line therefore exibits its own signal-to-noise ratio determined by the amount of absorption. All lines with $S/N < 6$ were discarded to ensure that the fitting procedure was accurate. Since measurements were performed at four different column densities, at least two of the four spectra will contain a specific line unsaturated. The final line position is then averaged over these two measurements.

Assuming proper sampling Fourier-Transform spectroscopy provides an intrinsically linear frequency scale. Initially, calibrations were performed using as a reference the Ar $(3p)^5(^2\mathrm{P}_{\frac{3}{2}})9d[\frac{3}{2}] \leftarrow (3p)^6\,{}^1\mathrm{S}_0$ transition, known with an accuracy of 0.03 cm^{-1} [27]. However, during the analysis it was found that setting the FT spectrometer at different p parameters introduces small variations in the calibration branch geometry (see inset Fig.1). Because this effect introduces systematic errors of $\sim$ few $\times 10^{-7}$ a recalibration procedure was implemented, relying on the many HD lines in the spectrum that are known to an accuracy of 5×10^{-8} from laser based studies [10–12]. The recalibration led to a linear correction of the spectrum and an improvement on the accuracy of the frequency axis.

The statistical uncertainty of a line position in a FT-spectrum with noise is governed by the formula [28]:

$$\Delta\sigma \sim \frac{W}{\sqrt{N_w}} \cdot \frac{f}{S/N} \tag{1}$$

where W is the FWHM of the line, N_w represents the number of the experimental points determining the line (defined as number of points above the half maximum level), S/N is the signal to noise ratio for the specific line and f is a geometrical factor relating to how well the kernel function matches the line shape. In the case of room temperature gas cell spectrum of HD for the Lyman and Werner bands the Doppler effect completely determines the lineshape of the non-saturated lines. Then using typical values of $W \sim 0.8$ cm^{-1} , $N_w = 4$, $f \sim 1$ and $S/N > 6$ a statistical value of 0.07 cm^{-1} is estimated. However, this is a worst case estimation when the line is determined in only one scan with the worst S/N ratio. In practice we have at least two spectra measured at different column densities ensuring that at least one of them has a much higher S/N ratio. Another estimation of the statistical uncertainty can be derived from estimating the spread of the transitions of the Fourier spectrum with respect to the laser calibrated lines [10–12] (Δ^{L} in the tables). Such a comparison between data sets yields a standard deviation of 0.03 cm^{-1} for the deviations. As a conservative estimate we put 0.04 cm^{-1} as the standard deviation.

The R(J) and P($J+2$) transitions of a certain vibrational band probe the same rotational level of the upper state. These combination differences can be compared with the high-precision far-infrared data from the quadrupole spectrum [26] and used for verification. Based on the 0.04 cm^{-1} uncertainties for single lines the estimated uncertainties for the combination differences amount to 0.06 cm^{-1}. Fig. 3 shows that the present results are consistent and fall well within these error margins. It can be seen that combination differences constructed from weaker lines

(R(3) - P(5)) result in larger scatterring around the true value.

In Tables 2 and 3 the fourth column Δ^{D} represents the deviations between the present data with those of Dabrowski and Herzberg. For lower energies up to $B - X(17,0)$ the difference of the present results with respect to the previous is negative with an average value of -0.23 cm^{-1}, while for higher energies it is positive with an average value of 0.17 cm^{-1}. The sudden change at $B - X(17,0)$ can also be observed in [9]. The linearity of the FTS and the independant observations by Hinnen with laser spectroscopy suggest that this change may be the result of the calibration procedure in the classical studies.

The present results were compared with the data of Hinnen *et al.* [9]. On average a systematic offset of 0.06 cm^{-1} is found, while in few cases the difference reaches 0.12 cm^{-1} which is outside the estimated error margin. The error estimation of 0.035 cm^{-1} in [9] was overly optimistic; later it was found that the I_2-reference calibration was offset by 0.06 cm^{-1} due to the fact that only a single spatial mode of the multimode laser beam was used in the calibration procedure in our laboratory. The $B - X(17,0)$ R(3) line was excluded in the analysis due to an unrealistically large difference of 1 cm^{-1}, possibly due to a typo in [9]. Calibration problems also led to a reassignment of $B - X(13,0)$ R(2) to the $EF - X(6,0)$ band in [9]; in the present study it is shown that the initial assignment by Dabrowski and Herzberg [8] was correct. With the present results the combination difference involving this line lies well within the estimated value (see Figure 3).

Table 1.: Transition energies (in cm^{-1}) for lines in the Lyman bands of HD. The estimated uncertainty is 0.04 cm^{-1}(1σ) except for some very weak or blended lines. Δ^{L} and Δ^{D} represent differences of the present values with the previously reported by laser [10–12] and classical [8] spectroscopy respectively. The last column contains the sensitivity coefficient for each transition to a possible variation of the proton-to-electron mass ratio. Lines marked with *b* were blended in the spectrum.

This work		Δ^{L}	Δ^{D}	K_i	This work		Δ^{L}	Δ^{D}	K_i
$B - X(0,0)$									
R(0)	90 428.96	0.01		-0.00654					
R(1)	90 398.19	0.00		-0.00695	P(1)	90 310.38	0.00		-0.00790
R(2)	90 307.55	0.05		-0.00811	P(2)	90 161.86			-0.00969
R(3)	90 157.53			-0.00987					
$B - X(1,0)$									
R(0)	91 574.94	-0.04		-0.00038					
R(1)	91 541.65	-0.01		-0.00084	P(1)	91 457.69	-0.02		-0.00173
R(2)	91 447.22	0.00		-0.00203	P(2)	91 307.91	0.00		-0.00347
R(3)	91 292.31	0.01		-0.00384	P(3)	91 098.59	0.01		-0.00590
R(4)	91 078.00			-0.00609	P(4)	90 831.11			-0.00864
$B - X(2,0)$									
R(0)	92 692.90	-0.02		0.00528					
R(1)	92 657.39	-0.02		0.00483	P(1)	92 576.74			0.00407
R(2)	92 559.69			0.00359	P(2)	92 425.83	-0.02		0.00224
R(3)	92 400.55			0.00175	P(3)	92 214.30			-0.00014
R(4)	92 181.08			-0.00050	P(4)	91 943.60			-0.00290
$B - X(3,0)$									
R(0)	93 784.41	0.03	-0.39	0.01061					
R(1)	93 746.89		0.59	0.01014	P(1)	93 669.17	-0.02		0.00940
R(2)	93 646.31	-0.02	-0.49	0.00888	P(2)	93 517.30	-0.01	-0.13	0.00763
R(3)	93 483.39	0.00	-0.13	0.00703	P(3)	93 303.85	0.02	-0.11	0.00525
R(4)	93 259.26	0.00	-0.18	0.00474	P(4)	93 030.25	0.01	-0.13	0.00251
R(5)	92 975.56		-0.11	0.00177					
$B - X(4,0)$									
R(0)	94 850.22	-0.02	-0.54	0.01557					
R(1)	94 811.00			0.01505	P(1)	94 735.92	-0.03	-0.28	0.01435
R(2)	94 707.77		-0.23	0.01379	P(2)	94 583.19	0.01	-0.38	0.01263
R(3)	94 541.37		-0.22	0.01188	P(3)	94 367.92		-0.14	0.01024
R(4)	94 312.99		-0.57	0.00958	P(4)	94 091.68		0.01	0.00751
R(5)	94 024.26		-0.04	0.00665					

continue on the next page

This work		Δ^{L}	Δ^{D}	K_i	This work		Δ^{L}	Δ^{D}	K_i
$B - X(5,0)$									
R(0)	95 891.06	-0.01	-0.24	0.02013					
R(1)	95 850.19[b]	0.02	-0.61	0.01959	P(1)	95 777.59	-0.01	-0.31	0.01898
R(2)	95 744.52	0.03	-0.38	0.01832	P(2)	95 624.01	0.01	-0.29	0.01724
R(3)	95 574.84	-0.01	-0.16	0.01644	P(3)	95 407.13	0.05	-0.07	0.01486
R(4)	95 342.49	-0.03	0.49	0.01411	P(4)	95 128.38		-0.22	0.01214
R(5)	95 049.15		0.15	0.01113	P(5)	94 789.74		0.14	0.00880
$B - X(6,0)$									
R(0)	96 907.23	0.01	-0.27	0.02439					
R(1)	96 864.77[b]	0.01	-0.53	0.02389	P(1)	96 794.54	0.01	-0.23	0.02325
R(2)	96 756.80	0.02	-0.50	0.02255	P(2)	96 640.17	0.03	-0.23	0.02154
R(3)	96 584.11	0.00	-0.34	0.02065	P(3)	96 421.72			0.01922
R(4)	96 348.08	0.03		0.01831	P(4)	96 140.71		-0.09	0.01647
R(5)	96 050.31		0.01	0.02231	P(5)	95 799.01		-0.19	0.01313
$B - X(7,0)$									
R(0)	97 899.04	0.00	-0.47	0.02831					
R(1)	97 855.13	0.01	-0.31	0.02778	P(1)	97 787.10	0.00	-0.40	0.02722
R(2)	97 744.94[b]	0.00	-0.67	0.02644	P(2)	97 631.96	-0.01	-0.53	0.02550
R(3)	97 569.39	0.01	-0.11	0.02452	P(3)	97 412.01	-0.02	-0.39	0.02318
R(4)	97 329.80	0.03		0.02217	P(4)	97 128.84		-0.17	0.02045
R(5)	97 027.90		-0.17	0.02298	P(5)	96 784.41		-0.10	0.01711
$B - X(8,0)$									
R(0)	98 866.80	-0.01		0.03193					
R(1)	98 821.46	0.02	-0.21	0.03138	P(1)	98 755.59[b]	-0.01		0.03087
R(2)	98 709.15	0.00	-0.33	0.03007	P(2)	98 599.73	-0.01	-0.31	0.02915
R(3)	98 530.80	-0.02	-0.30	0.02809	P(3)	98 378.35	-0.01		0.02684
R(4)	98 287.77[b]	-0.05		0.02575	P(4)	98 093.07			0.02416
R(5)	97 981.89		-0.20	0.02854					
$B - X(9,0)$									
R(0)	99 810.94	0.00	-0.25	0.03530					
R(1)	99 764.34	0.00	-0.20	0.03472	P(1)	99 700.36	0.00	-0.24	0.03425
R(2)	99 650.20	0.01	-0.32	0.03337	P(2)	99 543.88		-0.18	0.03256
R(3)	99 469.46		-0.44	0.03140	P(3)	99 321.22	-0.03	-0.33	0.03024
R(4)	99 223.72	-0.01	-0.15	0.02895	P(4)	99 034.04[b]			0.02753
R(5)	98 917.88[b]			0.03040	P(5)	98 684.47		-0.04	0.02418
$B - X(10,0)$									
R(0)	100 731.64[b]		-0.46	0.03836					
R(1)	100 683.60		-0.40	0.03779	P(1)	100 621.74		-0.20	0.03734
R(2)	100 567.38		-0.22	0.03647	P(2)	100 464.56		-0.04	0.03565
R(3)	100 383.88		-0.26	0.03449	P(3)	100 240.49		-0.23	0.03337
R(4)	100 134.54		-0.36	0.03206	P(4)	99 951.28		-0.19	0.03070
R(5)	99 820.95[b]		-0.31	0.03378	P(5)	99 598.95		-0.04	0.02736
$B - X(11,0)$									
R(0)	101 624.40		-0.29	0.04119					
R(1)	101 581.01		0.82	0.04055	P(1)	101 518.29		0.76	0.04018
R(2)	101 463.13		-0.55	0.03913	P(2)	101 357.37		0.01	0.03852
R(3)	101 278.70		-0.34	0.03678	P(3)	101 137.92			0.03618
R(4)					P(4)				
R(5)	100 703.29		0.08	0.03580	P(5)	100 493.71			0.02973
$B - X(12,0)$									
R(0)	102 503.53			0.04376					
R(1)	102 453.02[b]		-0.45	0.04316	P(1)	102 394.91		-0.43	0.04261
R(2)	102 332.80		-0.36	0.04179	P(2)	102 236.45		-0.35	0.04112
R(3)	102 147.32		-0.18	0.03982	P(3)	102 009.93		-0.22	0.03883
R(4)	101 890.90[b]			0.03744	P(4)	101 716.76		-0.17	0.03616
R(5)	101 570.43		-0.12	0.03812					
$B - X(13,0)$									
R(0)	103 356.32		0.14	0.04606					
R(1)	103 305.85		-0.41	0.04519	P(1)	103 247.83		-0.47	0.04512
R(2)	103 191.57		-0.05	0.04035	P(2)	103 089.23		-0.63	0.04345
R(3)	102 985.10		-0.04	0.03877	P(3)	102 862.81		-0.33	0.04091
R(4)	102 725.62		-0.33	0.03902	P(4)	102 575.48		-0.08	0.03475
R(5)	102 409.26			0.03986					
$B - X(14,0)$									
R(0)	104 186.14		-0.34	0.04821					
R(1)	104 133.52		-0.13	0.04762	P(1)	104 078.65[b]			0.04725
R(2)	104 010.40		-0.32	0.04623	P(2)	103 919.09		-0.52	0.04562

continue on the next page

This work		Δ^{L}	Δ^{D}	K_i	This work		Δ^{L}	Δ^{D}	K_i
R(3)	103 817.85		-0.24	0.04422	P(3)	103 690.49		-0.34	0.04338
R(4)	103 557.02		-0.26	0.04182	P(4)	103 394.35		-0.18	0.04072
$B - X(15, 0)$									
R(0)	104 992.05		-0.85	0.04653					
R(1)	104 938.50		-0.81	0.04828	P(1)	104 887.83			0.04919
R(2)	104 814.05		-0.35	0.04753	P(2)	104 724.97		-0.30	0.04396
R(3)	104 619.74[b]			0.04576	P(3)	104 495.39		-0.05	0.04408
R(4)	104 357.09[b]			0.04350	P(4)	104 197.97[b]			0.04207
R(5)	104 027.40		-0.07	0.04314					
$B - X(16, 0)$									
R(0)	105 781.66	-0.02	0.12	0.05186					
R(1)	105 727.07	0.00		0.05128	P(1)	105 675.13[b]	0.02	0.16	0.05095
R(2)	105 601.02	-0.02	0.49	0.04987	P(2)	105 514.62	0.01	-0.08	0.04932
R(3)	105 404.63	-0.01	-0.17	0.04786	P(3)	105 284.03	0.04		0.04712
R(4)	105 139.53[b]		-0.30	0.04536	P(4)	104 984.94		-0.22	0.04447
$B - X(17, 0)$									
R(0)	106 546.11		0.43	0.05333					
R(1)	106 490.13[b]			0.05269	P(1)	106 440.31		0.15	0.05252
R(2)	106 362.16		0.15	0.05124	P(2)	106 278.99		0.45	0.05081
R(3)	106 163.30[b]		0.37	0.04924	P(3)	106 047.04			0.04856
R(4)	105 895.13[b]			0.04682	P(4)	105 746.06		0.31	0.04588
$B - X(18, 0)$									
R(0)	107 292.96		0.15	0.05477					
R(1)	107 236.54		0.20	0.05416	P(1)	107 187.30		0.14	0.05389
R(2)	107 107.80		0.14	0.05273	P(2)	107 025.90		0.13	0.05227
R(3)	106 908.03		0.18	0.05067	P(3)	106 793.48		0.26	0.05007
R(4)					P(4)	106 491.81			0.04741
$B - X(19, 0)$									
R(0)	108 017.12		0.47	0.05596					
R(1)	107 959.24		0.35	0.05529	P(1)	107 912.30		0.47	0.05510
R(2)	107 828.45		0.40	0.05387	P(2)	107 750.11		0.42	0.05349
R(3)	107 625.82		0.42	0.05181	P(3)	107 516.17		0.37	0.05123
R(4)	107 352.90		0.38	0.04939	P(4)	107 212.34		0.34	0.04860
$B - X(20, 0)$									
R(0)	108 721.84[b]		0.12	0.05698					
R(1)	108 663.84		0.26	0.05634	P(1)	108 617.08		0.26	0.05611
R(2)	108 532.89			0.05484	P(2)	108 454.82		0.41	0.05452
R(3)	108 330.69[b]		0.51	0.05256	P(3)	108 220.76[b]			0.05231
					P(4)	107 916.77		0.66	0.04961
$B - X(21, 0)$									
R(0)	109 406.64[b]		-0.04	0.05786					
R(1)	109 346.46		0.24	0.05721	P(1)	109 302.00[b]		0.24	0.05700
R(2)	109 213.09		0.28	0.05579	P(2)	109 139.02		0.36	0.05542
R(3)	109 007.01			0.05374	P(3)	108 903.33[b]		0.35	0.05321
R(4)	108 729.80		0.35	0.05127	P(4)	108 596.69[b]			0.05059
$B - X(22, 0)$									
R(0)	110 071.36		0.36	0.05855					
R(1)	110 012.15		0.31	0.05778	P(1)	109 967.22		0.34	0.05775
R(2)	109 880.65		0.32	0.05570	P(2)	109 804.25		0.24	0.05613
R(3)					P(3)	109 569.08[b]			0.05381
R(4)	109 376.84		0.36	0.04924	P(4)	109 264.50		0.33	0.05053
$B - X(23, 0)$									
R(0)	110 715.06		0.00	0.05915					
R(1)	110 654.10			0.05849	P(1)	110 611.67		-0.19	0.05831
R(2)	110 518.46[b]		0.85	0.05707	P(2)	110 448.01		0.57	0.05674
R(3)	110 309.35		0.53	0.05502					
R(4)	110 028.28		0.40	0.05250					
$B - X(24, 0)$									
R(0)	111 347.02		-0.10	0.05895					
R(1)					P(1)	111 242.51			0.05877
R(2)	111 138.09		0.05	0.05439	P(2)	111 080.02		0.29	0.05656
R(3)	110 930.39		0.30	0.05442	P(3)	110 851.28		0.36	0.04838
R(4)	110 649.65		0.50	0.05246					
$B - X(25, 0)$									
R(0)	111 955.75		-0.13	0.05989					
R(1)	111 893.57[b]		-0.10	0.05919	P(1)	111 853.85[b]		0.36	0.05905

continue on the next page

This work		$\Delta^{\rm L}$	$\Delta^{\rm D}$	K_i	This work		$\Delta^{\rm L}$	$\Delta^{\rm D}$	K_i
R(2)	111 757.99		-0.11	0.05777	P(2)	111 688.70		-0.02	0.05751
R(3)	111 541.22		-0.06	0.05568	P(3)	111 450.51		-0.05	0.05530
$B - X(26, 0)$									
R(0)	112 541.15		-0.06	0.05975					
R(1)	112 476.57		-0.21	0.05898	P(1)	112 440.10		-0.22	0.05922
R(2)	112 336.43		-0.21	0.05758	P(2)	112 274.05		-0.24	0.05738
R(3)	112 121.84		-0.15	0.05556	P(3)	112 033.43		-0.23	0.05510
R(4)	111 834.16		-0.21	0.05314					
$B - X(27, 0)$									
R(0)	113 112.48		0.27	0.06004					
R(1)	113 048.26		0.16	0.05933	P(1)	113 010.15		0.04	0.05921
R(2)	112 907.91[b]		-0.13	0.05785	P(2)	112 845.38		0.22	0.05768
R(3)	112 692.66		0.06	0.05571	P(3)	112 605.12		-0.06	0.05548
$B - X(28, 0)$									
R(0)									
R(1)	113 598.48		-0.01	0.05907	P(1)				
R(2)	113 456.06		0.30	0.05759	P(2)	113 397.16		0.28	0.05747
R(3)	113 238.14		0.38	0.05549					
$B - X(29, 0)$									
R(0)	114 198.02		-0.04	0.05951					
R(1)	114 132.33		-0.08	0.05882	P(1)	114 097.04		-0.12	0.05871
R(2)	113 989.70		-0.54	0.05728	P(2)	113 930.94		-0.07	0.05717
					P(3)	113 689.27		0.12	0.05500
$B - X(30, 0)$									
R(0)	114 711.98		0.09	0.05898					
R(1)	114 644.87		0.15	0.05825	P(1)	114 611.72		-0.03	0.05823
R(2)	114 500.52			0.05673	P(2)	114 444.83		-0.06	0.05665

4. Calculation of the sensitivity coefficients

The present experimental investigation on the spectroscopy of HD is motivated by the possibility to include these lines in a search for a variation of the proton-electron mass ratio on a cosmological time scale [10]. In recent years HD lines have been observed in quasar absorption spectra at high redshift [4, 5], and in the most recent study on the J2123 system at redshift $z = 2.05$ HD lines are included in addition to H_2 lines to derive a constraint on $\Delta\mu/\mu$, where $\Delta\mu$ is the difference between proton-to-electron mass ratio in the present epoch $\mu_0 = m_p/m_e$ (at zero redshift) and the mass ratio μ_z for the absorbing cloud (at high redshift z) [6]. An important ingredient for such an analysis is the knowledge of the so-called sensitivity coefficients, defined as [15, 17]:

$$K_i = \frac{d(ln\lambda_i)}{d(ln\mu)} = \frac{\mu}{\lambda_i}\frac{d\lambda_i}{d\mu} = -\frac{\mu}{\sigma_i}\frac{d\sigma_i}{d\mu} \qquad (2)$$

where $\lambda_i = 1/\sigma_i$ and $\sigma_i = E_i^{up}(v', J') - E_i^{low}(v'', J'')$ is the transition frequency. These K_i coefficients determine how much each spectral line shifts as a result of a possible variation in μ corresponding to:

$$\frac{\lambda_i^z}{\lambda_i^0} = (1 + z_{abs})(1 + \frac{\Delta\mu}{\mu}K_i) \qquad (3)$$

with z_{abs} the overall redshift of the absorbing hydrogen cloud, λ_i^z the transition wavelength at high redshift and λ_i^0 the wavelength in the laboratory frame (zero redshift).

Table 1. Transition energies (in cm^{-1}) for lines in the Werner bands of HD. The estimated uncertainty of all transitions is 0.04 cm^{-1}(1σ). $\Delta^{\rm L}$ and $\Delta^{\rm D}$ represent differences of the present values with the previously reported by laser [10–12] and classical [8] spectroscopy respectively. The last column contains the sensitivity coefficient for each transition to a possible variation of the proton-to-electron mass ratio.

This work		$\Delta^{\rm L}$	$\Delta^{\rm D}$	K_i	This work		$\Delta^{\rm L}$	$\Delta^{\rm D}$	K_i	This work		$\Delta^{\rm L}$	$\Delta^{\rm D}$	K_i
C(v=0)														
R(0)	99 276.28	0.02	-0.68	-0.00391										
R(1)	99 279.88	0.02	-0.25	-0.00389	Q(1)	99 186.39	0.01	-0.33	-0.00486					
R(2)	99 240.47	-0.02	-0.29	-0.00441	Q(2)	99 100.14	0.00	0.00	-0.00589	P(2)	99 009.18	0.00	-0.23	-0.00677
R(3)	99 158.41	0.01		-0.00529	Q(3)	98 971.63		-0.14	-0.00726	P(3)	98 836.76	-0.03		-0.00857
R(4)	99 032.36			-0.00627	Q(4)	98 801.81	-0.02		-0.00880	P(4)	98 624.40	0.01	-0.25	-0.01051
R(5)					Q(5)	98 592.04		-0.16	-0.01078	P(5)	98 373.33		-0.15	-0.01282
C(v=1)														
R(0)	101 289.54[b]			0.00562										
R(1)	101 289.54[b]			0.00559	Q(1)	101 199.80			0.00467					
R(2)	101 243.53		-0.52	0.00507	Q(2)	101 109.49		-0.58	0.00359	P(2)	101 022.66			0.00284
R(3)	101 152.28		-0.17	0.00450	Q(3)	100 974.85			0.00219	P(3)	100 846.23			0.00105
R(4)	101 002.18		0.14	0.01675	Q(4)	100 796.90		-0.34	0.00056	P(4)	100 627.41			-0.00085
R(5)					Q(5)	100 576.98		-0.06	-0.00152	P(5)	100 367.27		-0.10	-0.00280
C(v=2)														
R(0)	103 201.94		-0.19	0.01381										
R(1)	103 196.68		0.73	0.01402	Q(1)	103 112.24		0.50	0.01286					
R(2)	103 140.20		-0.40	0.01685	Q(2)	103 017.84		-0.88	0.01177	P(2)	102 934.86		0.18	0.01111
R(3)	103 056.65		-0.04	0.01532	Q(3)	102 877.20		-0.12	0.01030	P(3)	102 753.58			0.00960
R(4)	102 909.43		-0.65	0.01139	Q(4)	102 691.29		-0.21	0.00859	P(4)	102 524.13		-0.09	0.01111
R(5)	102 719.69		-0.12	0.00928	Q(5)	102 461.51			0.00645	P(5)	102 271.56			0.00823
C(v=3)														
R(0)	105 018.45		-0.58	0.02434										
R(1)	105 010.26		-0.36	0.02186	Q(1)	104 925.58		-1.13	0.01987					
R(2)	104 953.13		-0.50	0.02055	Q(2)	104 827.24			0.01875	P(2)	104 751.40			0.02171
R(3)	104 847.31		-0.38	0.01914	Q(3)	104 680.69		-0.01	0.01722	P(3)	104 567.18		-0.27	0.01755
R(4)	104 693.38		-0.32	0.01765	Q(4)	104 487.03		-0.23	0.01544	P(4)	104 337.10		-0.06	0.01493
R(5)	104 492.03		-0.05	0.01585	Q(5)	104 247.40		-0.13	0.01320	P(5)	104 062.30		-0.10	0.01221
C(v=4)														
R(0)	106 731.61		0.02	0.02667										
R(1)	106 719.94		0.10	0.02656	Q(1)	106 641.22		0.17	0.02573					
R(2)	106 657.23		0.05	0.02582	Q(2)	106 539.02		0.14	0.02459	P(2)	106 464.53		0.38	0.02408
R(3)	106 543.53		0.10	0.02462	Q(3)	106 386.60		0.08	0.02299	P(3)	106 276.79		0.04	0.02234
R(4)	106 379.16		0.24	0.02331	Q(4)	106 185.13		0.44	0.02119	P(4)	106 041.10			0.02032
R(5)					Q(5)	105 935.89		0.36	0.01886	P(5)	105 758.51		0.29	0.01784
C(v=5)														
R(0)	108 349.85		0.26	0.03148										
R(1)	108 333.86		0.33	0.03126	Q(1)	108 259.75		0.29	0.03056					
R(2)	108 264.59		0.41	0.03053	Q(2)	108 153.69		0.37	0.02940	P(2)	108 082.75		0.49	0.02895
R(3)	108 141.72			0.02948	Q(3)	107 995.45		0.44	0.02775	P(3)	107 890.75		0.49	0.02712
R(4)	107 961.79		0.68	0.02978	Q(4)	107 786.23		0.40	0.02586	P(4)	107 648.46		0.43	0.02514
R(5)	107 686.60		0.60	0.03137	Q(5)	107 527.48		0.47	0.02346					

continue on the next page

Table 1. continued...

This work		Δ^L	Δ^D	K_i	This work		Δ^L	Δ^D	K_i	This work		Δ^L	Δ^D	K_i
C(v=6)														
R(0)	109 871.21		0.15	0.03528										
R(1)	109 850.40		0.11	0.03512	Q(1)	109 781.47		0.11	0.03441					
R(2)	109 772.96		0.11	0.03488	Q(2)	109 671.44		0.10	0.03319	P(2)	109 604.16		0.29	0.03280
R(3)	109 629.39		0.25	0.03933	Q(3)	109 507.41		0.23	0.03153	P(3)				
R(4)	109 477.83		0.35	0.03378	Q(4)	109 290.46		0.22	0.02956	P(4)	109 156.85		0.36	0.02959
					Q(5)	109 021.84			0.02706					
C(v=7)														
R(0)	111 294.07			0.03868										
R(1)	111 261.05			0.04435	Q(1)	111 205.51			0.03725					
R(2)	111 199.89		0.50	0.03991	Q(2)	111 091.55		0.17	0.03602	P(2)	111 026.96		0.05	0.03623
R(3)	111 060.02		0.13	0.03637	Q(3)	110 921.59		0.50	0.03431	P(3)	110 817.86		-0.08	0.04037
R(4)	110 865.93		-0.12	0.03409	Q(4)	110 696.84		-0.03	0.03221	P(4)	110 583.77		-0.13	0.03472
					Q(5)	110 418.59		0.39	0.02964					
C(v=8)														
R(0)	112 621.21		-0.45	0.04019										
R(1)	112 594.09		0.12	0.03992	Q(1)	112 530.27		0.14	0.03911					
R(2)	112 507.62		0.16	0.03887	Q(2)	112 412.34		0.36	0.03782	P(2)	112 354.08		-0.07	0.03777
R(3)	112 362.23			0.03723	Q(3)	112 236.35		-0.06	0.03601	P(3)	112 150.94		0.02	0.03597
R(4)	112 158.17		-0.27	0.03541	Q(4)	112 003.52		-0.15	0.03388	P(4)	111 891.52		-0.19	0.03373
C(v=9)														
R(0)														
R(1)	113 811.18		0.01	0.04040	Q(1)	113 753.07		0.11	0.03993					
R(2)					Q(2)	113 630.93		-0.14	0.03860	P(2)				
R(3)	113 563.36			0.03782	Q(3)	113 448.76		0.52	0.03674	P(3)	113 368.09		0.18	0.03650
R(4)	113 346.81		0.34	0.03632	Q(4)	113 207.64		0.25	0.03451	P(4)				
C(v=10)														
R(0)	114 959.56		-0.25	0.04045										
R(1)	114 922.83		0.15	0.04001	Q(1)	114 869.71		0.32	0.03966					
R(2)	114 822.46			0.03896	Q(2)	114 743.22		0.30	0.03829	P(2)	114 692.45		-0.01	0.03809
R(3)	114 657.07		0.08	0.03760	Q(3)	114 554.48		0.11	0.03634	P(3)	114 479.73		0.07	0.03614
R(4)					Q(4)	114 304.66		0.04	0.03397	P(4)				

The K_i coefficients have previously been calculated for H_2 through semi-empirical methods [15, 17] and via first principles calculations [18]. Here we adopt the method of calculating the coefficients, by solving the Schrödinger equation for ground and excited states using *ab initio* potentials to derive level energies and transition wavelengths. The sensitivity coefficient for a given line is calculated as the derivative of its wavelength or of its wavenumber with respect to the mass ratio μ. Thus, the first step is to calculate energies of the upper levels of transitions belonging to excited electronic states and energies of lower levels belonging to the ground electronic state. These energy levels are obtained by solving the Schrödinger equation of the ro-vibrational motion in a given electronic state. The second step is to calculate wavenumbers as differences between level energies, then to derive wavelengths of transitions. These steps in the calculations are repeated for several values of the mass ratio μ chosen to be close to the mass ratio of the present epoch. The results allow the determination of the derivative of the wavelength of a given line with respect to μ. At present the proton-to-electron mass ratio measured by Mohr and Taylor [29] with a relative accuracy of 2×10^{-9} is equal to $\mu_0 = 1836.15267247(80)$. This value was taken as the central value for determining the K_i.

4.1. *Calculation of level energies*

In the present case, the wavelengths of interest are those of electronic transitions between ro-vibrational levels of the $B^1\Sigma_u^+$, $C^1\Pi_u$, $B'^1\Sigma_u^+$, $D^1\Pi_u$ excited states and of the ground electronic state $X^1\Sigma_g^+$. The four excited states B, B', C and D states are well known to be strongly coupled and it is necessary to go beyond the adiabatic approximation. The principle of the present level calculations is similar to the one described in the study of the D_2 VUV emission spectrum [30]. Using high accuracy *ab initio* adiabatic potentials and taking into account the radial couplings between the B and $B'^1\Sigma_u^+$ sates and between the C and $D^1\Pi_u$ states, as well as the $(\Sigma^+ - \Pi^+)$ rotational couplings, we performed calculations of energies of the upper bound levels belonging to these states, by solving a system of four radial coupled equations, given in matrix form as :

$$\{-\frac{1}{2\mu_n}[\mathbf{I}\frac{d^2}{dR^2} - \mathbf{I}\frac{J'(J'+1)}{R^2} + \mathbf{A}(R) + 2\mathbf{B}(R)\frac{d}{dR}] + \mathbf{U}(R) - E\}\,\varphi(R) = 0 \quad (4)$$

where μ_n is the reduced mass of the HD nuclei given by:

$$\mu_{HD} = \frac{m_p \times m_D}{m_D + m_p} \quad (5)$$

and m_D is the deuterium nucleus mass. In atomic units, the mass unit is m_e, then the proton-to-electron mass ratio μ is numerically equal to m_p in atomic units used in our calculations. $\mathbf{I}$ is the identity matrix and $\mathbf{U}(R)$ is the diagonal matrix of adiabatic potential curves. The diagonal elements of the $A(R)$ matrix are the adiabatic corrections, whereas the off-diagonal elements involve both non adiabatic couplings between states of the same symmetry ($\Sigma-\Sigma$ or $\Pi-\Pi$) and the rotational couplings between $\Sigma - \Pi$ states, and finally $B(R)$ is the radial coupling matrix. More details for the formalism are described by Senn *et al.* [31]. The potential energy curves and relevant parameters for the excited states were taken from the work of Wolniewicz and coworkers [32–34].

The $\varphi(R)$ is the eigenvector matrix containing the expansion coefficients $\varphi_i(R)$ of the total ro-vibrational wave function of the molecule in the adiabatic basis of

the electron-rotational wave functions. In the present case, the nonadiabatic wave function $\varphi_i(R)$ is a four-component vector :

$$\varphi_i(R) = \{\varphi_{n,i}(R), \varphi_{n',i}(R)...\}. \quad (6)$$

The label n refers to the particular electronic state belonging to $\{B, B', C, D\}$, and the label i is an ordering index according to increasing energies.

It is convenient to transform the coupled equations by a unitary transformation which makes the first derivative radial coupling vanish. In the transformed equations, written in the so-called diabatic representation, the matrix of the hamiltonian has diagonal elements given by diabatic potentials, which may cross even between states of same symmetry, and off-diagonal elements given by electronic couplings between the diabatic states with no radial derivatives. We used, in the present study, the Fourier Grid Hamiltonian (FGH) method [31], an efficient and accurate method for bound state problems, to solve the coupled equations, as well as the one-state Schrödinger equation (see below eq.9). The advantage of this method is to provide all the energy values and the coupled-channel wave functions in one single diagonalisation of the Hamiltonian matrix expressed in a discrete variable representation (DVR). As the rotational interaction only affects the Σ^+ and Π^+ states, a system of coupled equations without rotational coupling has to be solved for the Π^- component. After solving the diabatic coupled equations, the solutions were transformed back to the adiabatic representation for the four-component $\varphi_i(R)$. The percentage of the electronic character n is obtained by :

$$\rho_i(n) = \int [\varphi_{n,i}(R)]^2 \mathrm{d}R. \quad (7)$$

with the normalisation : $\rho_i(B) + \rho_i(C) + \rho_i(B') + \rho_i(D) = 1$.
The electronic component $\varphi_{n,i}(R)$ takes into account not only the bound vibrational states but also the vibrational continuum. The percentage corresponding to a particular vibrational state v_n of the electronic state n can be obtained by expanding over a set of vibrational functions $\varphi_{n,v}(R)$, solutions of the uncoupled equation for adiabatic state n :

$$\rho_i(n, v) = \left| \int \varphi_{n,v}(R)\varphi_{n,i}(R)\mathrm{d}R \right|^2. \quad (8)$$

The $X^1\Sigma_g^+$ ground state [35] is isolated from the other excited states, therefore its vibrational energy levels were calculated by solving the one Schrödinger equation (eq 9) for each rotational quantum number J'' in the adiabatic approximation adding the corresponding centrifugal term to the *ab initio* potential $U_x(R)$, which includes the adiabatic correction into the Born-Oppenheimer potential, computed by Wolniewicz [35]. The relativistic and the radiative corrections [36] were also taken into account in the present calculations.

$$\{-\frac{1}{2\mu_n}\frac{d^2}{dR^2} + \frac{J''(J''+1)}{2\mu_n R^2} + U_x(R) - E_x\}\,\varphi_x(R) = 0. \quad (9)$$

The weak effect of excited states of the symmetries $\Sigma_{g(u)}$ and $\Pi_{g(u)}$, which leads to the regular nonadiabatic shifts ΔE_x of the levels of the ground state $X^1\Sigma_g^+$, was taken into account by means of the semiempirical relations [37]:

$$\Delta E_x = E_{\Sigma_g} + E_{\Sigma_u} + J''(J''+1)(E_{\Pi_g} + E_{\Pi_u}) \tag{10}$$

Where:

$$E_{\Sigma_{g(u)}} = \frac{\langle \varphi_x | E_x^{ad} - V_x(R) | \varphi_x \rangle}{\mu_n} \sum_i a_i(\Pi_{g(u)}) \eta^i \tag{11}$$

$$E_{\Pi_g} = \frac{1}{\mu_n^2} \sum_i b_i(\Pi_g) \eta^i \tag{12}$$

$$E_{\Pi_g} = \frac{1}{\mu_\alpha^2} \sum_i b_i(\Pi_u) \eta^i \tag{13}$$

where μ_α is the difference of mass of the deuterium nucleus and the hydrogen nucleus given by: $\mu_\alpha = (m_D + m_p)/(m_D - m_p)$. η is a the mass-dependent quantum number given by: $\eta = (v_x + \frac{1}{2})/\sqrt{\mu_n}$. The energies $E_{\Sigma_{g(u)}}$ and $E_{\Pi_{g(u)}}$ belong, respectively, to the electronic states $\Sigma_{g(u)}$ and $\Pi_{g(u)}$. φ_x represents the ro-vibrational wave function associated to the energy E_x. $V_x(R)$ is the adiabatic energy potential of the ground state X including the centrifugal barrier. Here, the mass-independent coefficients a_i and b_i of the polynomial expansions were determined from the experimental energy levels for homonuclear isotopomers H_2, D_2, and T_2.

Similar calculations of the level energies were reported by Abgrall and Roueff [38] using the same *ab initio* data but different method to solve the Schrödinger equation. As previously mentioned we used the the Fourier Grid Hamiltonian method, based on a Discret Variable Representation (DVR) of the wavefunctions and of the Hamiltonian, while Abgrall and Roueff used the Numerov method. Our 4-state calculations led to the same energies as reported in [38] for all levels involved in the current study, with largest discrepancy being ± 0.01 cm^{-1} for some high vibrational levels.

It must be noted that the full effect of *ungerade* - *gerade* symmetry-breaking in HD is not accounted for. There exist specific levels that undergo a *u-g* interaction between $B^1\Sigma_u^+$ and $C^1\Pi_u$ states on the one hand and $EF^1\Sigma_g^+$ states on the other hand (with a selection rule $\Delta J = 0$) giving rise to perturbations and level mixings. These effects are not included in our close coupling calculations because only incomplete *ab initio* coupling operators are available [**?**]. In order to estimate this effect a tentative calculation was performed for the example of the $B - X(25, 0)$ R(3), one of the most strongly affected lines. This yields a shift of 5.11 cm^{-1} and an increase in the sensitivity coefficient by approximately 7% induced by the EF coupling. An extended analysis of this *u-g* symmetry-breaking effect will be the subject of a future study.

4.2. *Determination of $d\lambda_i/d\mu$*

From the level energies calculated above, the wavelengths of transitions can be deduced. The entire procedure described has to be performed for several values of the reduced mass of nuclei μ_n, involving several values of the proton-to-electron

mass ratio μ chosen to be close to μ_0. In these conditions, the variation of a given wavelength λ_i versus μ is close to linear and its slope represents the derivative $d\lambda_i/d\mu$.

In the previous investigations [17] on a possible variation of μ, the statistical analysis of the recent observations of spectroscopic features in cold hydrogen clouds in the line of sight of two quasar light sources (Q 0405-443 and Q 0347-383), based on highly accurate laboratory wavelength measurements of H_2 lines, led to an order of magnitude of 2×10^{-5} for $\Delta\mu/\mu$ over 12 Gyears. This sets the scale to deduce a value of the derivative $d\lambda_i/d\mu$; the variation step of μ should be chosen to obtain a few points within this interval. In our case the calculations have been performed for the present value of $\mu_0 = 1836.15267261$ and another six values of μ separated by 0.02 and spanning from $\mu = 1836.10267261$ to $\mu = 1836.20267261$.

$R(J)$, $P(J)$ and $Q(J)$ transitions were calculated for each of the values of μ mentioned above. Then for each transition, the variation of wavelength versus μ was plotted and its slope was calculated by a linear fit. The fit provides, together with the slope, the uncertainty of its determination, the standard deviation of the fit and finally the χ^2 value. In Fig.4 we show two examples of the variation in wavelength of $B^1\Sigma_u^+(v = 5) \leftarrow X^1\Sigma_g^+(v = 0)$ R(0) and $C^1\Pi_u(v = 0) \leftarrow X^1\Sigma_g^+(v = 0)$ P(4) transitions due to variation in μ , as well as their linear fits.

The values of the K_i coefficients and their uncertainties were then deduced from the calculated values of the slopes and their uncertainties using equation (4). For completeness sensitivity coefficients were calculated for all experimentally observed lines, even for those beyond the Lyman-cutoff at $\lambda < 91$ nm in which domain the molecular hydrogen lines cannot be observed under the usual astrophysical conditions of a high density of H I. The values for the resulting K_i coefficients are listed in Tables 1 and 2 with the molecular transition frequencies.

The range of values for the K_i-coefficients for the HD lines observable in high-redshifted objects lie in the range -0.01 to 0.05, similarly as in H_2. These values are small, *i.e.* much smaller than for the proposed experiments involving detection schemes of μ variation on a laboratory time scale [39, 40]. This is due to the fact that the Lyman and Werner lines are electronic transitions, while the electronic energy in molecules is nearly mass-independent (in so far as the Born-Oppenheimer approximattion holds). In the comparison with high-redhsift H_2 and HD lines the sensitivity for detection of μ variation comes from the extremely large intervals of $\sim 10^{10}$ years. The here presented K_i coefficients for HD were in fact already used in the treatment of data in the J2123 quasar object at redshift $z = 2.05$ [41].

5. Conclusions

We report on a Fourier tranform spectroscopic study of HD in the VUV spectral domain at $\lambda = 87 - 112$ nm. Some 268 transitions in the $B^1\Sigma_u^+(v' = 0 - 30) \leftarrow X^1\Sigma_g^+(v'' = 0)$ Lyman bands and 141 transitions in the $C^1\Pi_u(v' = 0 - 10) \leftarrow X^1\Sigma_g^+(v'' = 0)$ Werner bands were deduced from a quasi static gas sample using a novel VUV Fourier transfom spectrometer at the Soleil Synchrotron facility. The estimated accuracies of the wavelength calibration is 0.04 cm^{-1}, which is verified by ground state combination differences. Accuracies of $\Delta\lambda/\lambda \sim 4 \times 10^{-7}$ match the accuracies as typically obtained in high redshift observations of the same molecular lines. The calculated sensitivity coefficients make the data relevant for the investigations of possible variation of the fundamental constants on a cosmological time scale.

6. Acknowledgements

The authors acknowledge fruitful discussions with Dr. M. Vervloet and Dr. D. Bailly. The staff of SOLEIL is thanked for the support and for providing the opportunity to conduct measurements in campaigns in 2008 and 2009. The work was supported by the Netherlands Foundation for Fundamental Research of Matter (FOM). We are indebted to EU for its financial support via the Transnational Access funding scheme.

References

[1] G. Carruthers, Astrophys. J. **161**, L81 (1970).
[2] M. Aaronson, B. J.H. and M. C.F., Astrophys. J. **191**, L53 (1974).
[3] R. Carlson, Astrophys. J. **190**, L99 (1974).
[4] D.A. Varshalovich, A.V. Ivanchik, P. Petitjean *et al.*, Astron. Lett. **27**, 683–685 (2001).
[5] P. Noterdaeme, P. Petitjean, C. Ledoux *et al.*, Astron. & Astrophys. **491** (2), 397–400 (2008).
[6] A. Malec *et al.*, Mon. Not. Roy. Astron. Soc. *in press* 2009.
[7] A. de Lange, E. Reinhold and W. Ubachs, Intern. Reviews in Phys. Chemistry **21**, 257–275(19) (2002).
[8] I. Dabrowski and G. Herzberg, Can. J. Phys. **54**, 525 (1976).
[9] P. Hinnen, S. Werners, S. Stolte *et al.*, Phys. Rev. A **52** (6), 4425–4433 (1995).
[10] T.I. Ivanov, M. Roudjane, M.O. Vieitez *et al.*, Phys. Rev. Lett. **100** (9), 093007 (2008).
[11] U. Hollenstein, E. Reinhold, C.A. de Lange and W. Ubachs, J. Phys. B **39** (8), L195–L201 (2006).
[12] T.G.P. Pielage, A. de Lange, F. Brandi and W. Ubachs, Chem. Phys. Lett. **366** (5-6), 583 – 587 (2002).
[13] G.M. Greetham, U. Hollenstein, R. Seiler *et al.*, Phys. Chem. Chem. Phys. **5** (12), 2528–2534 (2003).
[14] W. Ubachs and E. Reinhold, Phys. Rev. Lett. **92** (10), 101302 (2004).
[15] E. Reinhold, R. Buning, U. Hollenstein *et al.*, Physical Review Letters **96** (15), 151101 (2006).
[16] J.A. King, J.K. Webb, M.T. Murphy and R.F. Carswell, Phys. Rev. Lett. **101** (25), 251304 (2008).
[17] W. Ubachs, R. Buning, K.S.E. Eikema and E. Reinhold, J. Mol. Spectrosc. **241** (2), 155–179 (2007).
[18] V.V. Meshkov, A.V. Stolyarov, A.V. Ivanchik and D.A. Varshalovich, JETP Lett. **83** (8), 303–307 (2006).
[19] http://www.synchrotron-soleil.fr/portal/page/portal/Recherche/LignesLumiere/DESIRS .
[20] A. Thorne, Physica Scripta **T65**, 31–35 (1996).
[21] N. de Oliveira, D. Joyeux, D. Phalippou *et al.*, Rev. Sci. Inst. **80** (4), 043101 (2009).
[22] N. de Oliveira *et al.*, to be published .
[23] N. de Oliveira, D. Joyeux, D. Phalippou *et al.*, AIP Conference Proceedings **879** (1), 447–450 (2007).
[24] O. Marcouille, P. Brunelle, O. Chubar *et al.*, AIP Conference Proceedings **879** (1), 311–314 (2007).
[25] B. Mercier, M. Compin, C. Prevost *et al.*, J. Vac. Sci. Technol. A **18** (5), 2533–2541 (2000).
[26] L. Ulivi, P. de Natale and M. Inguscio, Astrophys. J. **378**, L29–L31 (1991).
[27] M. Sommavilla, U. Hollenstein, G.M. Greetham and F. Merkt, J. Phys. B **35** (18), 3901–3921 (2002).
[28] S. Davis, M. Abrams and J. Brault, *Fourier transform spectrometry*, 1st ed. (Academic Press, Oxford, 2001), p. 149.
[29] P.J. Mohr, B.N. Taylor and D.B. Newell, Rev. Mod. Phys. **80** (2), 633 (2008).
[30] M. Roudjane, F. Launay and W.U.L. Tchang-Brillet, J. Chem. Phys. **125** (21), 214305 (2006).
[31] P. Senn, P. Quadrelli and K. Dressler, J. Chem. Phys. **89** (12), 7401–7427 (1988).
[32] L. Wolniewicz and K. Dressler, J. Chem. Phys. **88** (6), 3861–3870 (1988).
[33] L. Wolniewicz and G. Staszewska, J. Mol. Spectrosc. **220** (1), 45–51 (2003).
[34] G. Staszewska and L. Wolniewicz, J. Mol. Spectrosc. **212** (2), 208–212 (2002).
[35] L. Wolniewicz, J. Chem. Phys. **103** (5), 1792–1799 (1995).
[36] L. Wolniewicz, J. Chem. Phys. **99** (3), 1851–1868 (1993).
[37] C. Schwartz and R.J.L. Roy, J. Mol. Spectrosc. **121** (2), 420 – 439 (1987).
[38] H. Abgrall and E. Roueff, Astron. & Astrophys. **445** (1), 361 (2006).
[39] H.L. Bethlem, M. Kajita, B. Sartakov *et al.*, Eur. Phys. J. Special Topics **163**, 55–69 (2008).
[40] H.L. Bethlem and W. Ubachs, Faraday Disc. **142**, 25–36 (2009).
[41] A.L. Malec, R. Buning, M.T. Murphy *et al.*, to be published .

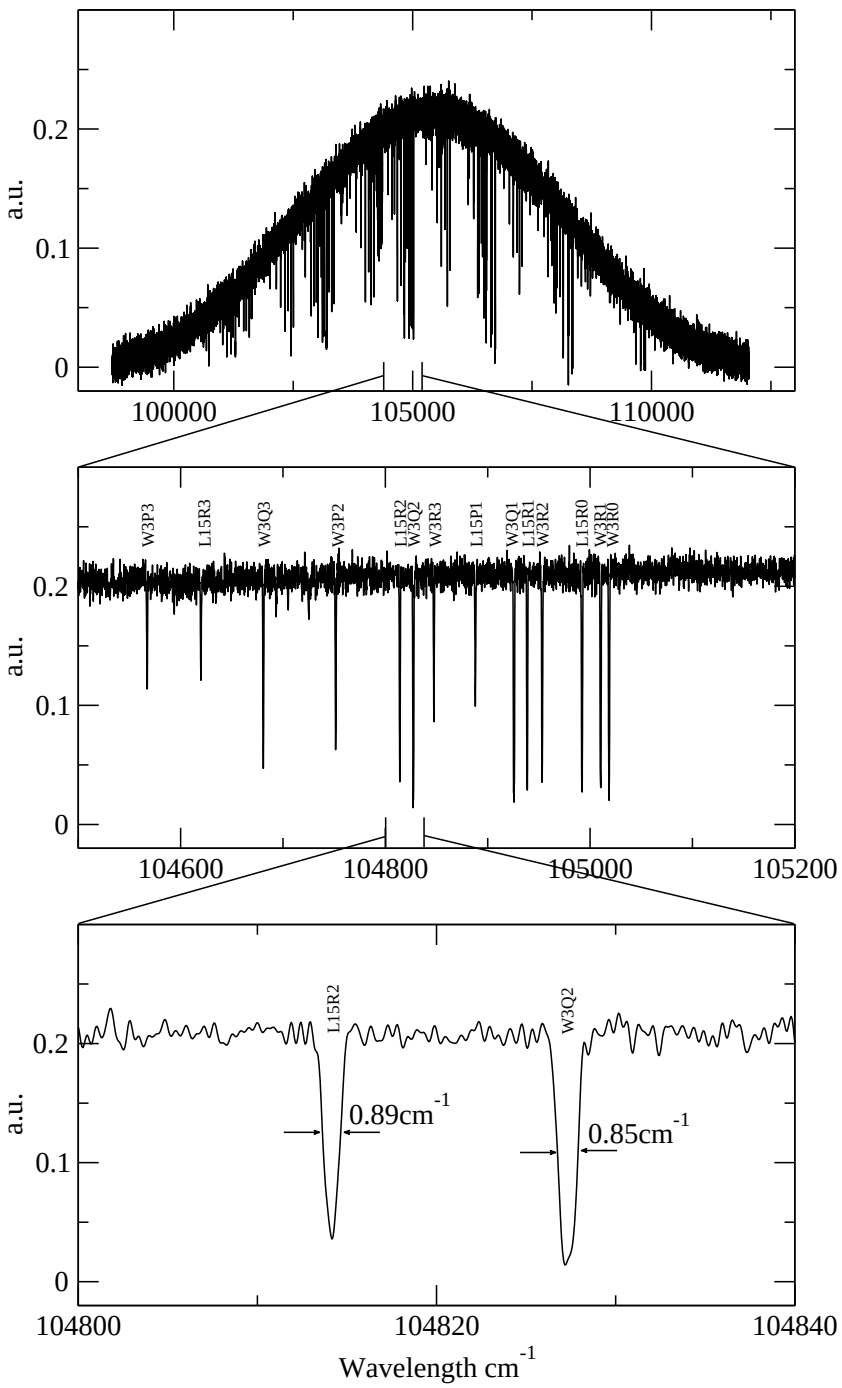

Figure 2. This spectrum represents one of the five windows covering the entire investigated spectral range - 90000-115000 cm^{-1}. It is a product of averaging 100 individual spectra. The Gaussian-like envelope represents the synchrotron radiation spectrum in which the absorption features of HD are encoded. The measurements were taken at room temperature and pressure at the input of the gas cell of 5.6×10^{-3} mbar. The bottom part of the figure focuses on a zoom on $B^1\Sigma_u^+$ $(v = 15) \leftarrow X^1\Sigma_g^+$ $(v = 0)$ R(2) and $C^1\Pi^-$ $(v = 3) \leftarrow X^1\Sigma_g^+$ $(v = 0)$ Q(2) transitions from Lyman and Werner band which are shortly labeled as L15R2 and W3Q2. It can be seen that the linewidths are determined by Doppler broadening. It should be noted also that for better visibility the spectrum has been interpolated.

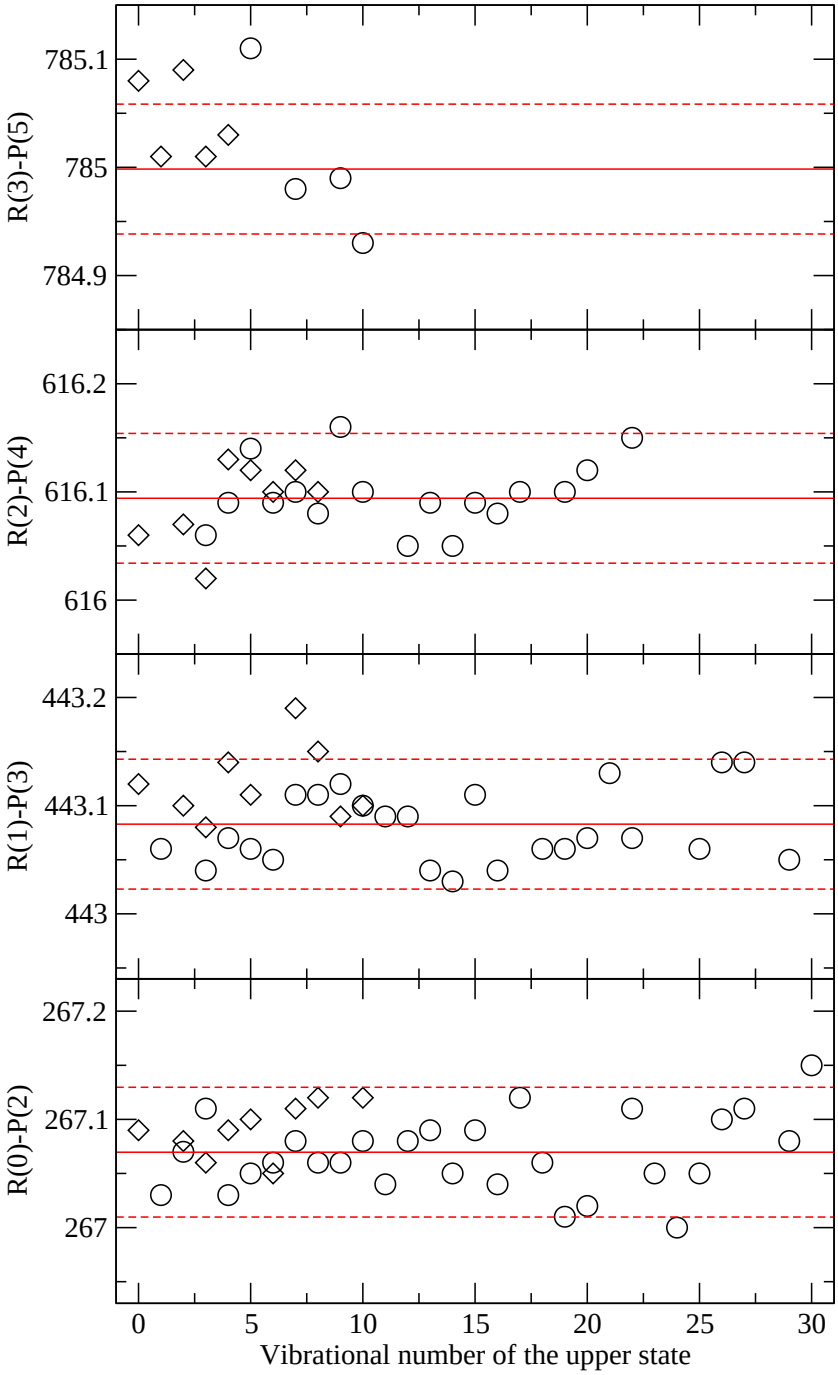

Figure 3. Combination differences, *i.e.* differences between R(J) and P($J+2$) transition frequencies, as constructed from the results of Table 2 and Table 3. Values are compared to the $\Delta J = 2$ splittings as accurately known from far-infrared FTS [26]; this is represented by the central line. The dashed lines indicate the estimated 1σ error bars of 0.06 cm^{-1}. The X axis represents the vibrational number of the upper state. Combination differences calculated from transitions belonging to the Lyman band are shown with circles, while the ones belonging to the Werner band are shown with diamonds.

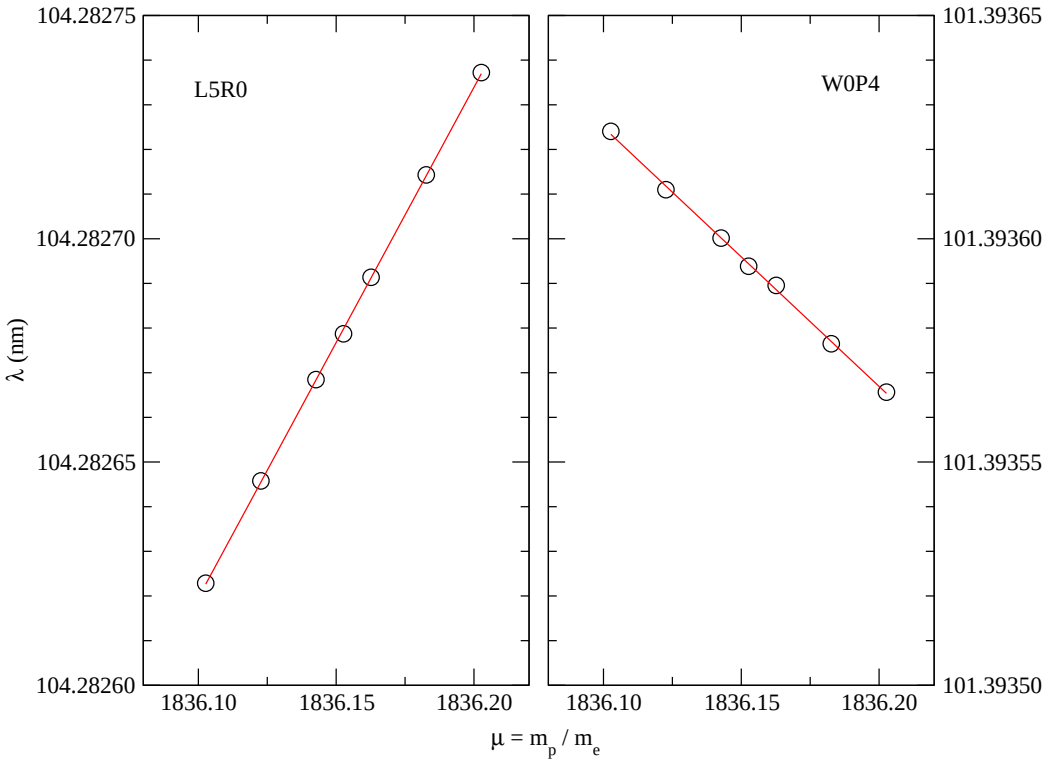

Figure 4. The wavelengths of the $B^1\Sigma_u^+$ $(v = 5) \leftarrow X^1\Sigma_g^+$ $(v = 0)$ R0 and $C^1\Pi^+$ $(v = 0) \leftarrow X^1\Sigma_g^+(v = 0)$ P4 transitions were deduced using calculations based on *ab initio* adiabatic potentials for seven different values of the proton-to-electron mass ratio around the presently known value. The sensitivity coeficients K_i are deduced from the slope of the linear regression of these points.